

Atomistic modeling of an Fe system with a small concentration of C

C.S. Becquart ^{a,*}, J.M. Raulot ^b, G. Bencteux ^c, C. Domain ^{a,d},
M. Perez ^e, S. Garruchet ^e, H. Nguyen ^a

^a *Laboratoire de Métallurgie Physique et Génie des Matériaux (LMPGM), Ecole Nationale Supérieure de Chimie de Lille, UMR 8517, Bat. C6, F-59655 Villeneuve d'Ascq Cedex, France*

^b *UMR CNRS 7078, Institut Supérieur de Génie Mécanique et Productique (ISGMP) Bat. B, Ile du Saulcy, F57045 Metz, Cedex 1, France*

^c *EDF – Recherche et Développement, Simulation en Neutronique, Technologie de l'information et Calcul Scientifique, 1, Avenue du Général de Gaulle, 92141 Clamart, France*

^d *EDF, Recherche et Développement, Matériaux et Mécanique des Composants, Les Renardières, F-77250 Moret sur Loing, France*

^e *Groupe d'Etudes de Métallurgie Physique et Physique des Matériaux (GEMPPM), INSA, UMR 5510, F-69621 Villeurbanne Cedex, France*

Received 22 September 2006; received in revised form 17 November 2006; accepted 20 November 2006

Abstract

An Fe–C potential based on the Embedded Atom Method has been derived, adjusted on ab initio data. This potential is dedicated to the study of ferritic FeC solid solutions for low carbon concentrations. This potential has been validated by checking its behaviour in the simulation of C diffusion in α -Fe and by determining the interaction of C atoms with a screw dislocation. The evolution of the matrix lattice parameter versus C content, related to the tetragonal lattice structure has also been evaluated as well as external stress effects on the diffusion energy barrier. The theoretical results are in good agreement with the experimental data available.

© 2006 Elsevier B.V. All rights reserved.

PACS: 61.72.–y; 61.72.jj; 61.72.Lk; 61.72.Yx; 62.20.Fe; 67.80.Mg

Keywords: FeC alloys; Interatomic potential; Screw dislocation; Ab initio calculations; Hetero-interstitial diffusion; Internal friction

1. Introduction

Carbon is one of the most frequent Foreign Interstitial Atoms (FIA) in the Fe matrix along with nitrogen atoms. Below its solubility limit, the presence of even a very little amount of these impurities in interstitial positions (a few tens ppm), can have a drastic influence on the steel properties, as they build strong interactions with the lattice defects present in the steel. It is well known that the interaction of C with dislocations and/or substitutional atoms has important effects on the yield stress and the subsequent mechanical properties of the materials.

To understand the role of C it is important to characterize its interaction with defects at the atomistic level. This can be done for instance by ab initio calculations [1,2] or using Molecular Dynamics in conjunction with empirical potentials or Monte Carlo simulations.

Some FeC empirical potentials have been derived in the past. Johnson et al. [3] derived two-body central potentials for the FeC systems. The metal–metal and the metal–carbon interactions are described by pairwise potentials (it is now widely agreed that pairwise interactions alone are not appropriate to model metal–metal interaction), and no carbon–carbon interactions was assumed. The Fe–C interaction potential was constructed such that the experimental carbon migration energy in Fe, and the activation volume for that migration, as well as the binding energy of a carbon vacancy dipole were reproduced by the model. Rosato [4] used a more realistic potential for

* Corresponding author. Tel./fax: +33 3 20 43 49 44.

E-mail address: Charlotte.Becquart@univ-lille1.fr (C.S. Becquart).

Fe, based on the tight binding second moment approximation, achieving a better calculation of elastic properties and a more natural agreement with experimental data. For the metal–metal potential he used for bcc Fe a Finnis–Sinclair model, [5] for fcc Fe a Rosato–Guillope–Legrand model [6]. The carbon–metal interaction is also described by a pair potential, and as the author aimed at studying the behaviour of a single C atom, he did not derive any carbon–carbon interaction.

More recently, Ruda et al. [7] derived an embedded atom method potential for FeC. The potentials were adjusted on ab initio calculations from the literature of the metastable carbide FeC in the B1 structure. The authors reproduced the equilibrium lattice constants, the bulk moduli and the cohesive energies for each of the stable and metastable carbides. However this potential finds the tetrahedral sites as energetically favoured, which is in contradiction with what is usually accepted or found theoretically [2].

One flaw of these potentials is that the Fe part of the model does not predict the correct structure of the screw dislocation core as well as the relative stability of the self interstitials.

Recently, ab initio calculations based on the Density Functional Theory (DFT), have been performed by Domain and co-workers [2] in the ferritic FeC system to determine the interactions of C atoms with one vacancy, the interaction between a self interstitial atom (SIA) and a C atom as well as the interactions between two C atoms. The diffusion properties of C were also investigated. Strong interactions of C atoms with one vacancy were obtained, whereas no significant interaction between the C atom was found with the SIA for the configurations investigated. As for the interaction between two C atoms, it was found to be repulsive for the three configurations explored, in which the C atoms were certainly too close to each other. Some of the configurations investigated in the work of Domain and co-workers [2] have been used in this work to parameterize an FeC potential dedicated to the study of ferritic FeC solid solutions for low C concentrations.

In the first part of this paper, the method used to derive the potential is described. In a second part, the newly derived potential is tested by confronting its prediction with the DFT based ab initio calculations of [2] as well as with other, unpublished ab initio results, also derived by ourselves.

In the third part, the potential is validated by molecular dynamics and molecular statics simulations. First, calculations of the carbon concentration influence on the iron matrix structure have been performed. Then, the carbon diffusion barrier at 0 K and the carbon diffusion coefficient for various temperatures has been determined. Next, in the purpose of using this potential to model the Snoeck peak (internal friction), the influence of stress on the carbon diffusion barrier has been investigated. Finally, the interaction of a screw dislocation with a single carbon atom positioned in different octahedral sites next to the dislocation is presented.

2. Methodology

2.1. The ab initio database

The ab initio calculations were performed using the Vienna Ab initio Simulation Package VASP [8–10]. They were done in a plane wave basis set, using fully nonlocal Vanderbilt-type ultrasoft pseudopotentials (USPP) to describe the electron–ion interaction [11]. Pseudopotentials simplify electronic-structure calculations by eliminating the need to include atomic core states and the hard potentials responsible for binding them. They allow also the use of a finite number of plane waves. Exchange and correlation were described by the Perdew and Zunger functional [12], adding nonlocal correction in the form of the Generalised Gradient Approximation (GGA) of Perdew et al. [13]. All the calculations were done with this functional. The pseudopotentials were taken from the VASP library. For Fe, the six 3d electrons are considered as valence ones together with the two 4s. For C, four valence electrons are used: 2s and 2p.

The supercell approach with periodic boundary conditions (PBC) was used to simulate point defects as well as pure phases. Brillouin zone (BZ) sampling was performed using the Monkhorst and Pack scheme [14]. The ion relaxations were performed using the standard Conjugate-Gradient algorithm implemented in the VASP code. For the solid solution calculations and the defect calculations, the relaxations were done at constant volume thus relaxing only the atomic positions in a supercell dimensioned with the equilibrium lattice parameter for Fe (2.8544 Å). This allows one to use a smaller plane wave cut-off energy and thus to speed up the calculations without altering the accuracy of the results. The plane wave cut-off energy was 290 eV. The error induced by this lower cut-off energy was checked to be negligible, as can be seen in a previous study of point defects structures in bcc Fe [15].

In all the results presented here, the number of k points (used to pave the Brillouin zone) is the total one and therefore not the number of irreducible k points. In all the tables, the “number of atoms” is more precisely the number of metallic atoms regular sites (as opposed to the number of interstitial sites) in the perfect supercell, i.e. the cell without any vacancies or Self Interstitial Atoms (SIA).

Most of the ab initio data have been published elsewhere [2], however, some unpublished results concerning in particular the interactions between two vacancies and one C atom as well as two C atoms and one SIA have been added to the ab initio database. Note that most of the ab initio configurations were used to validate the potential rather than to adjust it.

2.2. Construction of the potentials

The potentials were built according to the Embedded-Atom Method derived by Daw and Baskes [16,17] using

the ASSIMPOT software [18]. In this scheme, the total energy E_{tot} of a collection of atoms is given by

$$E_{\text{tot}} = \frac{1}{2} \sum_{i,j} \Phi_{ij}(r_{ij}) + \sum_i F_i \left(\sum_{j \neq i} \rho_j(r_{ij}) \right) \quad (1)$$

Here $\Phi_{ij}(r_{ij})$ is the pair-interaction energy between atoms i and j separated by the distance r_{ij} , F_i is the embedding energy of the atom i and $\bar{\rho}_i = \sum_{j \neq i} \rho_j(r_{ij})$ is the host electron density induced by the surrounding atoms j at the location of the atom i . The electron-density function assigned to atom j is $\rho_j(r_{ij})$. The pair interaction, electron-density and embedding functions depend on the atoms type. A description of a binary system Fe–C requires thus seven potential functions ($\Phi_{\text{FeFe}}(r)$, $\rho_{\text{Fe}}(r)$, $F_{\text{Fe}}(\bar{\rho})$, $\Phi_{\text{CC}}(r)$, $\rho_{\text{C}}(r)$, $F_{\text{C}}(\bar{\rho})$, $\Phi_{\text{FeC}}(r)$). These functions describe the atomic interactions in the pure α -Fe system, in the pure C system and the pair interactions between atoms Fe and C.

In the frame of ASSIMPOT, these functions are discretized on a mesh or projected on a finite number of functions (see below) and the fitting comes down to determining a finite set of coefficients that yields the minimal deviation between EAM model and the reference data. The optimization is realized with the algorithm derived by Broyden, Fletcher, Goldfarb and Shanno (BFGS algorithm) [19], thus the gradient of the computed properties with respect to the unknown parameters is needed. As this computation can become prohibitively costly in presence of a big number of unknowns, ASSIMPOT computes the so-called adjoint model [20,21], which keeps the cost of the gradient calculation independent of the number of unknowns.

There exist different strategies for generating a potential for binary systems. One is to employ good quality pure-Fe and pure-C potentials constructed separately and fit a cross potential $\Phi_{\text{FeC}}(r)$. The principal problem is that the number of parameters to fit to the properties of intermediate compounds is in our case limited. The other strategy is to optimize all seven potential functions simultaneously by fitting them to the whole set of data available for the system. This strategy provides more flexibility for selecting one compound and fitting its properties more accurately in comparison with other phases of the system.

As the purpose of the potential is to simulate dilute solid solutions, the interactions between C are not crucial and for instance the angular interactions do not need to be taken into account. A potential for α -Fe has been published recently [22] which has been adjusted on ab initio data and is nowadays commonly admitted to be the state of the art potential for this material. It was thus decided to use this Fe potential and to choose a combination of the first and the second approach, in the sense that during the building of the FeC potential the functions characterizing the pure-Fe potential ($\Phi_{\text{FeFe}}(r)$, $\rho_{\text{Fe}}(r)$, $F_{\text{Fe}}(\bar{\rho})$) were fixed, while all the other potential functions ($\rho_{\text{C}}(r)$, $F_{\text{C}}(\bar{\rho})$, $\Phi_{\text{FeC}}(r)$) were totally free to change.

2.3. Parametrization and fitting procedures

For the FeC interaction, the function was chosen to be a linear combination of truncated polynomials of degree 3, as in [23,24]:

$$\Phi_{\text{FeC}}(r) = \sum_{i=1}^n a_i H(b_i - r)(b_i - r)^3 \quad 1 \text{ \AA} \leq r \leq 3.502 \text{ \AA} \quad (2)$$

where H is the Heavyside function, and a_i and b_i the parameters gathered in Table 1. The advantage of this form of function is that it allows to act locally on the function while keeping global regularity.

For C atoms, the electron density was postulated to be of the form

$$\rho_{\text{C}}(r) = \sum_{i=1}^n c_i H(d_i - r)(d_i - r)^3 \quad 0 \text{ \AA} \leq r \leq 4.808 \text{ \AA} \quad (3)$$

where the c_i and d_i parameters are given in Table 2.

Finally, the embedding function was represented by the following function:

$$F_{\text{C}}(\rho) = F_1 \sqrt{\rho} + F_2 \rho^2 \quad (4)$$

where the parameters appear in Table 3.

As the potential aimed at simulating dilute solid solutions, no pair interaction between C atoms was derived.

The parameters were adjusted using the ASSIMPOT code and two ab initio configurations: one where the C

Table 1
Parameters of the cross Fe–C potential

I	a_i (eV/Å ³)	b_i (Å)
N		
1	25.8403449446387	1.57392207030071
2	12.1869023019844	1.64805018491946
3	5.29633693622809	2.50697533078414
4	4.03000262768764	2.55706258348374
5	−7.23257363478654	2.74993431502404
6	9.19127905165634	3.08003832563079
7	−7.91809159848018	3.11129997684853
8	0.283612435794859	3.50162017458081

Table 2
Parameters of the C electron density potential. a.u. means density arbitrary units

I	c_i (a.u./Å ³)	d_i (Å)
N		
1	−10.7034165597827	−41.4959151233716
2	−0.0964623684409615	4.80768853808491

Table 3
Parameters used in the C embedding function potential a.u. means density arbitrary units

Parameter	Value
F_1 (eV a.u. ^{−1/2})	−1.96195396340978
F_2 (eV a.u. ^{−2})	$9.88733654634282 \times 10^{-4}$

atom was in a tetrahedral configuration, the other one where the C atom was in an octahedral configuration. The ASSIMPOT code had to reproduce not only the energy of these configurations but also the forces acting on the atoms. At the end of the fitting procedure, the root-mean-square deviation on the forces was on the order of 10^{-2} eV/Å, while the relative error on the energies was on the order of 10^{-4} eV.

Furthermore, to make sure that the octahedral configuration was stable or more precisely metastable, the derivative of the energy versus the lattice parameter and the atomic positions at this precise location was compelled to be 0 during the fitting procedure.

3. Test of the potential: confrontations with other ab initio calculations

As stated above, the potential has only been adjusted on two ab initio configurations: one where the C atom was in a tetrahedral configuration, the other one where the C atom was in an octahedral configuration. In this paragraph, we now compare the prediction of the newly built potential with ab initio results not used in the fitting procedure.

Table 4 indicates the relaxation (in percent of $\Delta d_i/d_i^0$) around the C in the bcc structure as well as the C migration energy obtained by ab initio calculations, compared to the data obtained with the newly derived potential.

The experimental migration energy of C determined by resistivity measurements, positron-life time measurements or Snoek relaxation lies between 0.81 eV and 0.83 eV [25]. However, Takaki and co-workers by resistivity recovery of high purity and C doped iron finds a higher value of 0.88 eV [26] for a carbon atom in α -Fe. The ab initio data is in good agreement with the experimental results and the empirical potential agrees also with the experimental measurements, as it was adjusted on the tetrahedral and octa-

hedral configurations (the migration energy of C corresponds to the difference in energy between these two interstitial configurations).

Table 5 gathers the binding energies E_b for different configurations involving carbon atoms and/or vacancies and/or dumbbells. The binding energy $E_b(A_1, A_2)$ is defined as the difference of two system energies $E_{\text{noninterac}}$ and E_{interac} :

$$E_b(A_1, A_2) = E_{\text{noninterac}} - E_{\text{interac}}$$

In system *noninterac* A_1 and A_2 do not interact, i.e. they are situated far enough from each other not to interact. In system *interac*, A_1 and A_2 interact, and the distance between A_1 and A_2 may be first nearest neighbour distance, second nearest distance as well as other well defined configurations.

Because of the relatively small supercell sizes one has to use in the ab initio calculations, it is rather difficult to make sure that the two entities in system *noninterac* do not interact even when they are as far as the supercell size allows. Therefore another method has to be used to determine the binding energies. It consists in subtracting from the energy of system *interac* (where A_1 and A_2 interact), the energy of a system containing A_1 (calculated with a supercell with a size similar to that of system *interac*.) as well as that of a system containing A_2 (obtained with similar conditions) and that of the supercell with neither A_1 nor A_2 . For a supercell containing N atoms, the binding energy is thus obtained as

$$E_b(A_1, A_2) = [E(A_1) + E(A_2)] - [E(A_1 + A_2) + E_{\text{ref}}] \quad (5)$$

where E_{ref} is the energy of the supercell without A_1 and A_2 , $E(A_j)$ is the energy of the supercell containing A_j only and $E(A_1 + A_2)$ is the energy of the supercell containing both A_1 and A_2 in interaction with each other (i.e. the energy of system *interac* in the previous method). All the supercells contain the same number of metal sites, i.e. have the same size.

When more than two entities interact, the equation is generalised as follows:

$$E_b(A_1, A_2, \dots, A_n) = \sum_{i=1, \dots, n} E(A_i) - [E(A_1 + A_2 + \dots + A_n) + (n-1)E_{\text{ref}}] \quad (6)$$

Except when otherwise stated, the reference state of the binding energies presented in this work is always the energy of a supercell without any defects, i.e. a perfect crystal. With such a scheme a positive binding energy means attraction between the entities, while a negative binding energy indicates a repulsion.

The ab initio results for the vacancy–C binding energy (Table 5, configuration a) are in good agreement with the data obtained by Johnson (0.41 eV) [3,27] or by Rosato (0.48 eV) [4] with empirical potentials. However the comparison with experimental results is not straightforward as they are not always very coherent and arise from different techniques. Arndt and Damask [28] examining a neutron

Table 4
Relaxation (in percent of $\Delta d_i/d_i^0$) around the C in the bcc structure and C migration energy (eV)

	DFT–GGA: this work (128 atoms, 27 k points)	EAM: this work	Exp.
<i>Octahedral site</i>			
Relaxation of 1nn shell in percent of $\Delta d_i/d_i^0$	+24.3	+25.1	
<i>Octahedral site</i>			
Relaxation of 2nn shell in percent of $\Delta d_i/d_i^0$	–1.8	–2.2	
<i>Tetrahedral site</i>			
Relaxation of 1nn shell in percent of $\Delta d_i/d_i^0$	+13.9	+12.2	
<i>Tetrahedral site</i>			
Relaxation of 2nn shell in percent of $\Delta d_i/d_i^0$	–2.9	+0.06	
$E_{\text{migration}}$ (eV)	0.90	0.85	0.81–0.88 (see text)

Table 5

Binding energies. All the energies are in eV. The calculations except when marked with a superscript ‘a’ were done using 128 atom supercells and 27 *k* points

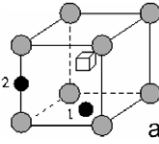
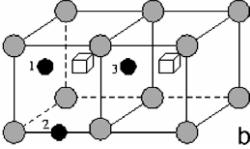
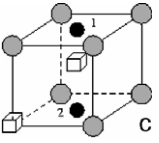
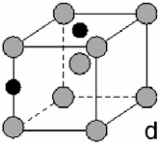
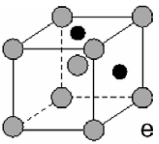
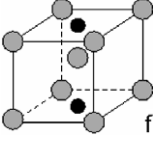
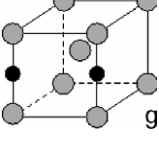
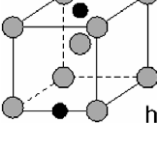
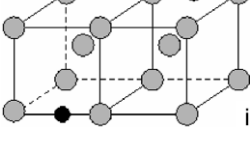
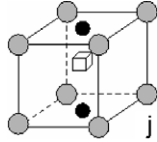
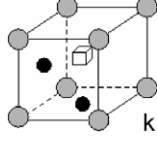
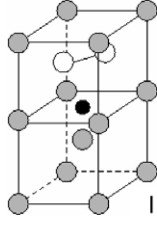
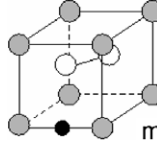
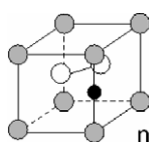
Configuration	DFT–GGA: this work	EAM: this work	Exp.
<i>One vacancy–one carbon atom</i>			
 a	+0.47(1) −0.01(2)	+0.83(1) −0.04(2)	0.41–1.1 (see text)
<i>Two vacancies–one carbon atom</i>			
 b	+0.34(1) +0.47(2) +0.68(3)	+1.06(1) +0.31(2) +0.90(3)	^a
 c	+0.58(1) +0.12 (2)	+0.99(1) +0.77(2)	^a
<i>Two carbon atoms</i>			
 d	−0.09	−0.16	
 e	−0.65	−0.50	
 f	−1.67	−0.96	
 g	−0.09	−0.11	
 h	+0.13	−0.05	
 i	+0.16	+0.05	

Table 5 (continued)

Configuration	DFT–GGA: this work	EAM: this work	Exp.
<i>One vacancy–two carbon atoms</i>			
 j	+1.07	+1.12	
 k	+1.50	+0.51	
<i>One SIA–one carbon atom</i>			
 l	−0.19	+0.40	
 m	−0.09	+0.26	
 n	−0.31	0.08	

^a Calculations done using 54 atom supercells and 125 *k* points.

irradiated Fe found by calorimetric measurements a large binding energy (0.41 eV) of C with a defect, which they postulated to be probably a vacancy. However, Wuttig et al. [29] examined by magnetic measurements the carbon and nitrogen trapping in Fe following low-temperature electron and neutron irradiation. They concluded that interstitial clusters formed during the low-temperature neutron irradiation acted as traps for carbon and nitrogen atoms, whereas vacancies were the trapping defects following electron irradiation. Little and Harries [30] also considered that the binding energy measured by Arndt and Damask [28] very likely corresponded to the binding energy of carbon to an interstitial cluster. On the other hand, Takaki and co-workers [26] doing careful resistivity measurements in very pure Fe and C doped Fe following low-temperature electron irradiation estimated that the binding energy of a carbon atom with a vacancy was 1.1 eV, while Vehanen [31] doing positron-lifetime measurements on electron-irradiated high purity and C doped Fe found 0.85 eV.

The newly derived potential reproduces fairly well the binding energy between a vacancy and a C atom in first and second nearest neighbour position, specially considering the scatter of the experimental results.

The configurations involving two vacancies and one C atom are in rather good agreement except for configurations *b1* and *c2* where the empirical potential gives too high energies as compared to the *ab initio* results.

When one introduces a second C in the α -Fe matrix, the most stable configuration appears to be when the atoms tend to lie as far away from one another as possible. This is consistent with the experimental observations that in the Iron–Carbon martensite the carbon atoms are as widely separated as possible [32]. The most repulsive configuration (the least stable) is when the two octahedral sites containing the FIAs are on top of each other, aligned along the shortest direction of the site, and thus along the most dilated direction.

The newly derived potential reproduces very well the *ab initio* data, in particular the trends except for configuration *h* where the empirical potential predicts a slight repulsion whereas the *ab initio* calculation indicates an attraction. It is important to note thus that, although the potential has been built with the aim of studying ferritic solid solution for low C concentrations, it models very satisfactorily the interactions between two C atoms situated not too far from each other.

The configurations involving one vacancy and two C atoms are in good agreement with the *ab initio* data except for the fact that the empirical potential is not able to reproduce the covalent bonding (and thus the increase in binding energy) which appears in the case where the two octahedral sites containing the C atoms are first neighbours [2]. This is not really surprising as the “shape” of the EAM potential cannot take into account such a covalent bonding which is directional while the mathematical form of the potential is completely spherical as can be seen in Eq. (1).

Takaki and co-workers [26] estimated the binding energy between a self interstitial atom and a carbon atom to be 0.11 eV. Earlier on, Johnson and Damask [33] calculated that an attractive binding energy of 0.5 eV existed between the $\langle 110 \rangle$ dumbbell and a carbon atom. In a previous paper [2], three configurations for the interaction between the SIA and the C atom were investigated. For all these configurations, a repulsion was observed. This appeared to be in disagreement with the experimental results mentioned above, but we are far from having explored all the possible configurations, and it is very probable that when the C atom lies further away from the SIA the interaction can be positive. When the C atom is close to the SIA, the newly derived potential fails to reproduce the *ab initio* calculations correctly as it always predicts an attraction between the two entities, while the *ab initio* indicates repulsion.

To conclude on this paragraph, the ability of the potential to reproduce *ab initio* results is fairly good. Let us stress out at this point, that the potential derived with

the method described in Sections 2.2 and 2.3, can only be used to study ferritic FeC solid solutions. Indeed, because the scheme adopted does not take into account triplets, it cannot reproduce the directional bonds expected when many C atoms gather together. Furthermore, this potential has been adjusted only on bcc configurations, and by no means can it be expected to treat austenitic alloys.

4. Validation of the potential

4.1. Lattice parameters of the tetragonal structure versus carbon content

The martensitic tetragonal structure provides an opportunity to test the potential as a function of increasing carbon content. Indeed, in the martensite, the carbon free bcc structure of pure iron is transformed to a body centred tetragonal structure, which lattice parameters *c* and *a* have been proven to vary linearly with the carbon concentration. In the bcc structure, carbon atoms remain in octahedral sites [34], which are strongly nonsymmetrical. This causes a considerable distortion of the crystal structure, an expansion in the direction of the two first neighbours and a contraction in the perpendicular direction of the four second neighbours.

Molecular dynamics simulations have been performed with the code LAMMPS [35] keeping the number of atoms, pressure and temperature constant (NPT) within periodic boundary conditions with one carbon atom in a ferrite matrix. The simulation box contained 128–2000 iron atoms. The simulations have been run until the system reaches an equilibrium at zero pressure. They have been made at room temperature (300 K) to compare the results obtained with those given by other authors. At this temperature, the potential gives a lattice parameter for pure iron (due to Ackland’s potential [22]) slightly lower (*a* = 0.2855 nm) than that obtained experimentally (*a* = 0.2866 nm). In Fig. 1, the simulated lattice parameters *c* and *a* are plotted as a function of carbon content. They are compared with those given by Cheng [36] from a review

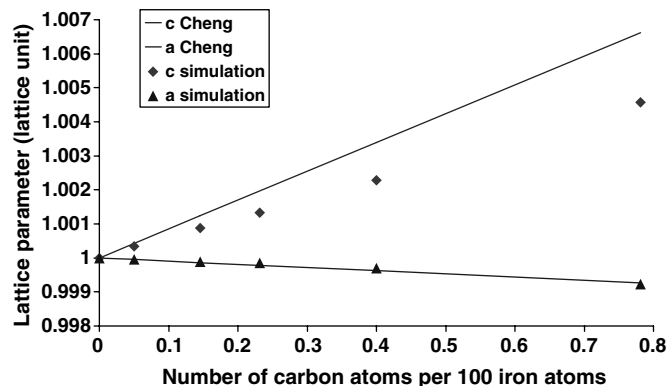


Fig. 1. Carbon composition dependence of the lattice parameters of the bcc iron martensitic phase. Cheng’s data [36] are scaled to the same origin as our results.

of many experimental measurements. The potential reproduces exactly the contraction of the lattice (parameter a), but underestimates its expansion in the other direction (parameter c), except for the very low carbon concentration. Nevertheless, the evolution of these lattice parameters is linear with carbon content. This potential thus reproduces quantitatively (within less than 0.25% error) the carbon induced transformation of the iron lattice from the carbon free centred cubic structure to the centred tetragonal structure.

4.2. Carbon diffusion in ferrite

Many important phenomena in materials science involve the diffusion of impurities. One example is carbon diffusion in iron. Due to its relatively high diffusivity, interstitial diffusion of carbon often controls the kinetics of phase transformations in steels and therefore the resulting microstructure. However, interstitial diffusion may cause problems such as strain aging, embrittlement, and steel erosion. Understanding the interstitial diffusion process in iron may help in understanding the behaviour of steel subject to different environments.

The carbon diffusion barrier at 0 K and the diffusion coefficient were calculated for different temperatures. A conjugate gradient minimisation procedure has been performed to compute the minimum energy path between octahedral sites. As expected, the carbon site energetically favoured is the octahedral site, as shown in Fig. 2, where the minimum energy path is plotted. Note that the transition state (saddle point) corresponds exactly to the tetrahedral site. Fig. 2 shows the minimum energy path and the iron atomic arrangement around the interstitial carbon. The carbon moves from the edge centre (0.0,0.5,0.0) to the other edge centre (1.0,0.5,0.0) via an octahedral and two tetrahedral sites. Note that Ruda et al. Fe–C potential [7] returns accurate mechanical properties but finds the tetrahedral sites as energetically favoured, which is in contra-

diction with what is usually accepted or found theoretically [2]. The value obtained for the diffusion barrier (0.85 eV) is in good agreement with experimental values [37–39] and quantum calculations [1,2].

In order to compare the carbon diffusion coefficient in bcc iron with experimental data, we also determined it for different temperatures (ranging from 850 K to 1150 K). In the NPT ensemble with 2000 iron atoms and 1 carbon atom, $n_{\max} = 2 \times 10^7$ MD steps were performed using a time step $\Delta t = 10^{-15}$ s (the boundary conditions were periodic and the pressure $P = 0$). The diffusion coefficient was then obtained from the mean square displacements using Einstein's relation: $6Dt = \langle |r(t) - r(0)|^2 \rangle$, where $r(t)$ is the position of the carbon atom at time t . The diffusion coefficient was computed from a running average with a 20 ns window. From the knowledge of the successive positions of the carbon atom $r(t_n) = r(n\Delta t)$, the mean square displacement is then given by: $\langle |r(t) - r(0)|^2 \rangle = \sum_{j=0}^{n_{\max}-n} |r((n+j)\Delta t) - r(j\Delta t)|^2 / (n_{\max} - n + 1)$. A run of 20 ns is long enough to obtain accurate statistics (i.e. a sufficient carbon jump number and a linear dependence of $\langle |r(t) - r(0)|^2 \rangle$ with time).

The diffusion coefficient follows an Arrhenius law,

$$D = D_0 \exp(-\Delta Q/k_B T) \quad (7)$$

where D_0 is the preexponential factor, ΔQ the diffusion barrier, k_B Boltzmann constant and T the temperature. In Fig. 3 the simulation results are compared with those obtained by Weller [38]. We notice a good agreement between the experimental data and the simulations. The calculated diffusion barrier $\Delta Q = 0.85$ eV is quite similar with the one obtained from the minimum energy path at 0 K, which is satisfactory. We also determined the preexponential factor for carbon diffusion D_0 which was found to be equal to $1.36 \times 10^{-6} \text{ m}^2 \text{ s}^{-1}$. This value remains within the average of those found in the literature ($D_0 = 2.0 \times 10^{-6} \text{ m}^2 \text{ s}^{-1}$ [38],

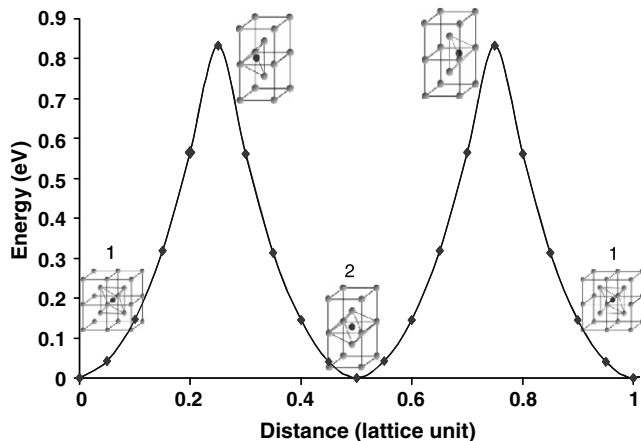


Fig. 2. Minimum energy path for carbon diffusion at 0 K. We can see the local structures of carbon atom (black atoms) in the iron matrix (light grey atoms); initial and intermediate states (octahedral sites 1 and 2) and transition states (tetrahedral sites).

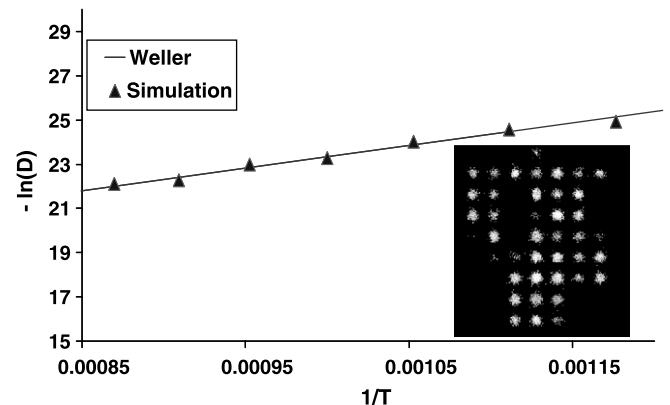


Fig. 3. Carbon diffusion coefficient as a function of the inverse of the temperature ($1/K$). The agreement between the calculated carbon diffusion coefficient (thanks to the running average technique) and the experimental values is remarkably good. The inset shows the projection of all the carbon positions (in the different octahedral sites of the iron matrix) at 850 K: 40 carbon jumps from one octahedral site to another octahedral site have been performed. This is consistent with an Arrhenius behaviour with an activation energy of 0.85 eV.

$3.94 \times 10^{-7} \text{ m}^2 \text{ s}^{-1}$, $1.67 \times 10^{-7} \text{ m}^2 \text{ s}^{-1}$ [25]), which vary by about one order of magnitude. Moreover, the inset in Fig. 3 shows the carbon positions in the iron matrix: it can be noticed, once again, that the carbon jumps from one octahedral site to another. All these results prove that our potential accurately reproduces carbon diffusion in ferrite.

4.3. Effects of external stress on the diffusion barrier

Stress has a strong effect on the interstitial diffusion in iron, due to the induced deformation of the interstitial sites. Furthermore, interstitial diffusion may cause phenomena such as internal friction, trapping of interstitial carbon on dislocation, etc. For these reasons, the influence of stress on the diffusion barrier has been investigated.

We first analysed the evolution of the energy barrier ΔQ (using a minimum energy path analysis) with the hydrostatic pressure applied to the system. The same conjugate gradient procedure as introduced in the preceding section has been applied to a system of 2000 iron atoms and 1 carbon atom with various simulation box sizes, leading to various hydrostatic pressures. Fig. 4 shows the linear dependence of the diffusion barrier with respect to the applied pressure. When a negative hydrostatic pressure is applied (as in the case of traction) to the system, the diffusion is faster, due to a decrease of the diffusion barrier. This is easily understandable, as the octahedral site becomes larger and accepts more readily an interstitial atom. Inversely, a positive hydrostatic pressure implies a slower diffusion, due to an increase of the diffusion barrier. Note that the negative pressure has a stronger influence on the carbon diffusion barrier.

Secondly, an uniaxial stress state was applied to the system, in order to study its influence on the diffusion barrier. The simulation box dimensions perpendicular to the traction axis (stress free directions) have been adjusted by minimizing the system energy, to get a uniform uniaxial stress state.

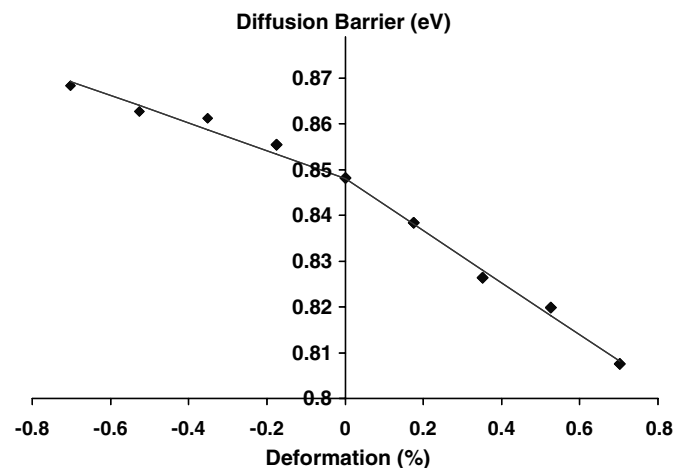


Fig. 4. Variation of the carbon diffusion barrier as a function of the deformation applied in each direction of the system.

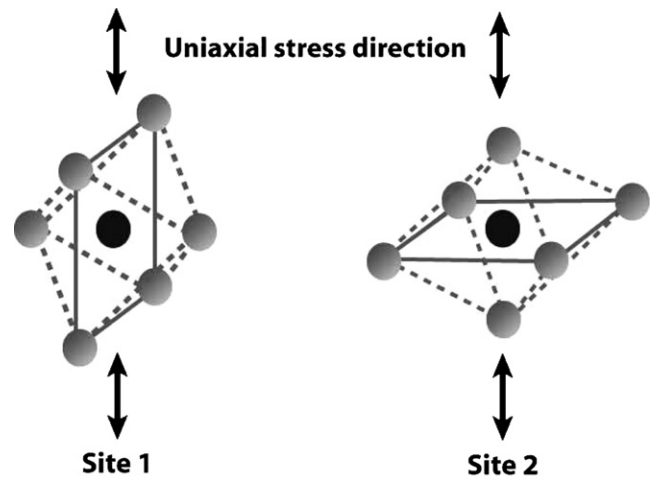


Fig. 5. The two octahedral site types for an interstitial carbon atom, and the direction of the uniaxial stress applied to the system. The traction axis can be either parallel (as in the case of site 1) or perpendicular (as in the case of site 2) to the square base of the octahedron. This square base is itself perpendicular to the shortest distance of the octahedron.

It can be noticed from Fig. 5 that under uniaxial stress, the carbon can be found in two types of octahedral sites (1 and 2) within the iron matrix. In type 1 (respectively type 2) sites, the direction containing the two first neighbours of a carbon atom is perpendicular (respectively parallel) to the traction axis (see (Fig. 5)). Note that under zero uniaxial stress state (or hydrostatic pressure), all the octahedral sites (1 and 2) are equivalent.

However, sites 1 and 2 will have different behaviours under uniaxial stress state. Fig. 6 shows the variation of the diffusion barrier when a carbon jumps from an octahedral site of type 1 to an octahedral site of type 2 (and respectively from an octahedral site of type 2 to an octahedral site of type 1) as a function of the applied deformation. As for the hydrostatic pressure, the diffusion barrier varies linearly with the deformation. Moreover, there is an energetically favoured site depending on the applied stress (traction or compression): site 1 is favoured under compression and site 2 is favoured under traction. Indeed, the two first neighbours of site 2 are moved aside under traction, leaving more space for the carbon atom.

Under uniaxial stress, the carbon atoms are no longer equally distributed in octahedral sites, this leads to an anelastic deformation, which can be measured in the so-called internal friction experiment, in which a cyclic uniaxial stress is applied and the carbon induced cyclic strain is determined [40]. By knowing the energy barrier variation as a function of applied stress, the present potential could thus be very useful to model the Snoek peak observed in internal friction experiments.

4.4. Interaction of C atom with a screw dislocation

In bcc metals, $1/2a\langle 111 \rangle$ screw dislocations are believed to control the low temperature plastic deformation because

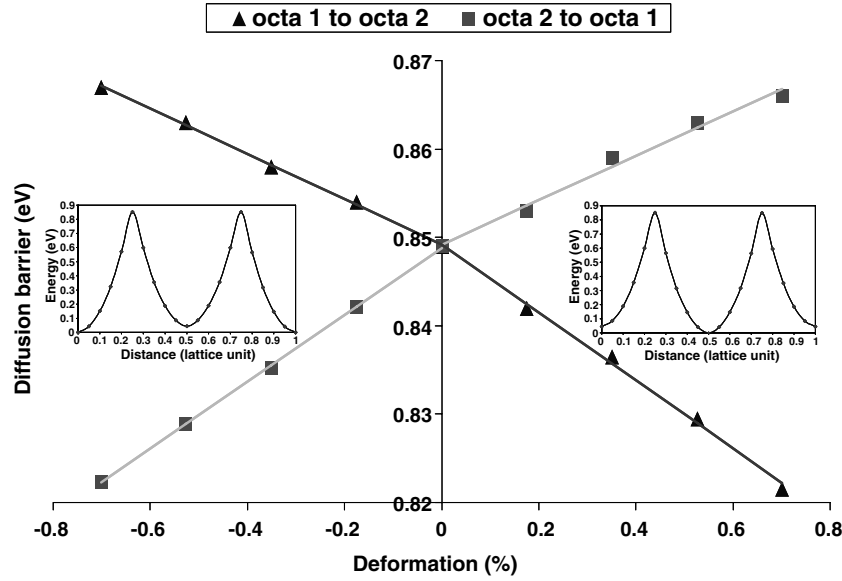


Fig. 6. Variation of the carbon diffusion barrier to jump from an octahedral site 1 to an octahedral site 2, respectively from an octahedral site 2 to an octahedral site 1 as a function of the deformation applied to the system during an uniaxial stress test. The inset shows the minimum energy path for the two extreme deformations.

their mobility is lower than that of edge dislocations. Therefore, it is of great interest to determine the activation energy required to move a dislocation. This energy barrier might be modified by defects in the crystal, and particularly by carbon in very dilute steels.

The core structure of the $1/2a\langle 111 \rangle$ screw dislocation in α -Fe has been examined using the differential displacement method [41] representation for atomic differential displacements. Let us recall that there are two possible configurations for $1/2a\langle 111 \rangle$ screw dislocations in bcc materials, corresponding to the so called “easy” and “hard” configurations [42]. The “easy” configuration was found to be more stable with our potential (for pure bcc Fe) than the “hard” one [43] and all “hard” screw dislocations thus relaxed into an “easy” one (Fig. 7). Note that the core is compact in agreement with ab initio results rather than exhibiting a degenerated core, asymmetrically spread in the three $\{110\}$ planes of the $[111]$ zone very often predicted by empirical potentials for Fe (usually referred to as threefold symmetry).

In the calculations, the bcc lattice is oriented such that the first axis lies along the $[\bar{1}\bar{1}2]$ direction, the second one along the $[1\bar{1}0]$ direction. Along the $[111]$ direction (which is parallel to the dislocation line) periodic boundary conditions were applied. Free surfaces have been imposed in the other directions to avoid self-interaction of the dislocation. The screw dislocation line was placed at the geometric centre of a triangle and because of its long-range interaction with surfaces, the simulation box used was a cylinder of 39,060 atoms, which axis was parallel to the dislocation line, $27\vec{b}$ long, and which radius measured approximately $16\vec{b}$. Note, that another simulation made using a larger box containing 90900 atoms, i.e. $30\vec{b}$ long and with a radius of $28\vec{b}$ did not predict any significant changes in

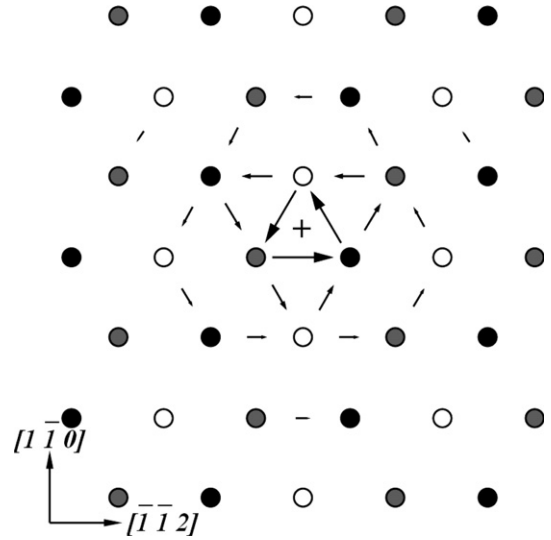


Fig. 7. Relaxed configuration of an “easy” screw dislocation core using Vitek’s differential displacement method [41]. The mathematical position of the core is indicated by the plus sign. The length of an arrow is proportional to the displacement difference. The longest arrow corresponds to $b/3$ and arrows shorter than $b/20$ are omitted for clarity. The different sphere colours indicate on which $\{111\}$ plane the atoms lie.

the binding energies between the screw dislocation and the octahedral interstitial.

The binding energy between the C atom and the dislocation has been determined employing molecular statics, using the DYMOKA code, and the following formula:

$$E_b(\text{screw}, \text{octa}) = [E(\text{screw}) + E(\text{octa})] - [E(\text{screw} + \text{octa}) + E_{\text{ref}}] \quad (8)$$

where $E(\text{screw})$ is the total energy of the system containing one screw dislocation, $E(\text{octa})$ the total energy of the

system containing one carbon atom in an octahedral site, $E(\text{ref})$ the total energy of the perfect lattice, and $E(\text{screw} + \text{octa})$ the total energy of the system containing both one dislocation and a carbon atom. As is the case for the point defect interactions, a positive binding energy indicates attraction between the interstitial and the dislocation.

The whole system has been relaxed using the quench algorithm [44].

The C atoms have been introduced in the neighbourhood of the dislocation line, in octahedral sites, after an initial relaxation of the dislocation. Except for the three sites the closest to the line (sites 21, 22 and 28 in Fig. 8), where the deformation induced by the screw dislocation is severe,

all the sites remain very likely within an octahedral geometry. In this figure, the octahedral sites are coloured following a scheme depending on their binding energy. A preliminary look at the results indicate that the sign of the binding energy depends on the orientation of the octahedral site with respect to the dislocation line. A more thorough discussion will be presented elsewhere.

Fig. 9 represents the relaxed binding energy versus distance to the dislocation line. The final configurations of the dislocation core is shown for each binding energy.

It is worth noting that the maximum binding energy found here is 0.41 eV close to the value of 0.5 eV found by Kamber et al. by use of anelastic measurements (Snoek

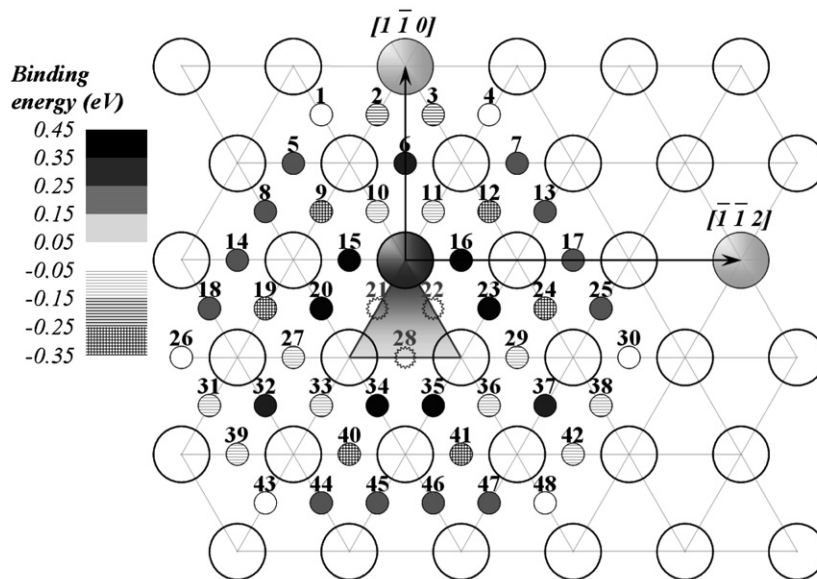


Fig. 8. Labelling of the different octahedral sites investigated. The octahedral sites are coloured following a scheme depending on their binding energy.

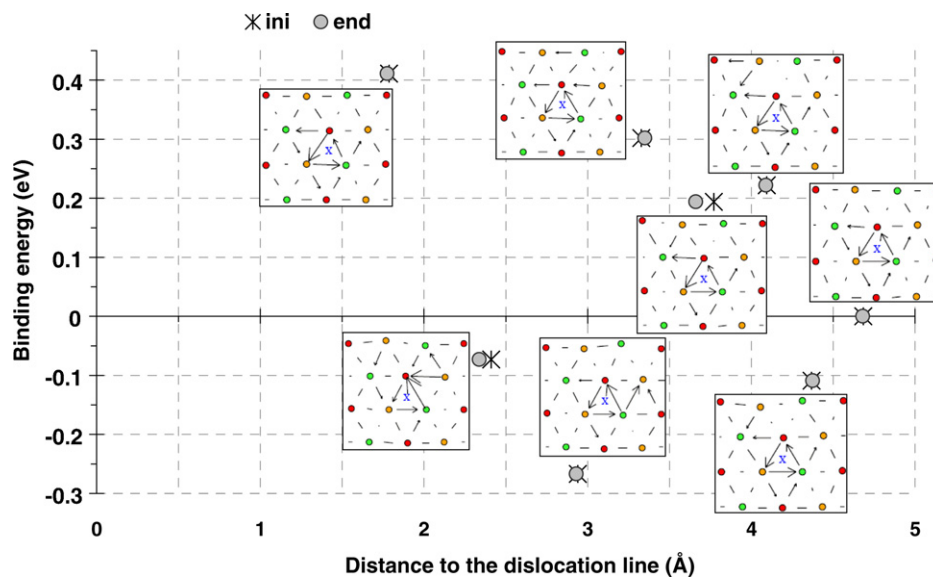


Fig. 9. Evolution of the C–dislocation binding energy versus distance to the line. The distance is taken between the final position of the C atom after relaxation and the initial position of the line (filled circle). Indeed after relaxation, as the core in many cases spreads out, the position of the line is more difficult to visualise. The initial distance between the C atom before relaxation and the line is marked by a star. The pictures associated to each binding energy show the final configuration of the core. The initial mathematical position of the core is indicated by a cross.

damping peak and the cold-work damping peak) [45]. Cochardt and co-workers [46] obtained a higher value of 0.75 eV however they used an elastic theory which thus did not take into account the chemical part of the interaction. Our results are thus in very good agreement with the experimental data.

5. Conclusions

An Fe–C potential dedicated to the study of ferritic FeC solid solutions for low C concentrations has been derived, adjusted on ab initio data. Using this potential the diffusion coefficient of C in α -Fe and the interactions of C atoms with a screw dislocation have been determined. The evolution of the microstructure with the C amount has also been investigated. All the results obtained with the newly derived potential are in good agreement with the experimental data. Preliminary data pertinent in the modeling of internal friction Snoek peak have also been obtained.

Acknowledgements

This work has been performed within the European PERFECT project (FI6O-CT-2003-508840) which has sponsored this study. This research has been done using the CRI supercomputer of the USTL supported by the Fonds Européens de Développement Régional, as well as the CEA CCRT supercomputers in the framework of an EDF-CEA contract.

References

- [1] D.E. Jiang, E. Carter, Phys. Rev. B 67 (2003) 214103.
- [2] C. Domain, C.S. Becquart, J. Foct, Phys. Rev. B 69 (2004) 144112.
- [3] R.A. Johnson, G.J. Dienes, A.C. Damask, Acta Metall. 12 (1964) 1215.
- [4] V. Rosato, Acta Metall. 37 (1989) 2759.
- [5] F. Finnis, J.E. Sinclair, Philos. Mag. A 50 (1984) 45.
- [6] V. Rosato, M. Guillope, B. Legrand, Philos. Mag. A 59 (1989) 321.
- [7] M. Ruda, D. Farkas, J. Abriata, Scripta Mater. 46 (2002) 349.
- [8] G. Kresse, J. Hafner, Phys. Rev. B 47 (1993) 558;
- [9] G. Kresse, J. Hafner, Phys. Rev. B 49 (1994) 14251.
- [10] G. Kresse, J. Furthmüller, Phys. Rev. B 54 (1996) 11169.
- [11] G. Kresse, J. Furthmüller, Comput. Mater. Sci. 6 (1996) 15.
- [12] D. Vanderbilt, Phys. Rev. B 41 (1990) 7892;
- [13] G. Kresse, J. Hafner, J. Phys.: Condens. Mater. 6 (1996) 8245.
- [14] J.P. Perdew, A. Zunger, Phys. Rev. B 23 (1981) 5048.
- [15] J.P. Perdew, J.A. Chevary, S.H. Vosko, K.A. Jackson, M.R. Pederson, C. Fiolhais, Phys. Rev. B 46 (1992) 6671.
- [16] H.J. Monkhorst, J.D. Pack, Phys. Rev. B 13 (1976) 5188, In the original Monkhorst and Pack scheme, the *k*-point mesh is always symmetric around the γ point, whereas very often in our calculations we adopted grids centered at the γ point.
- [17] C. Domain, C.S. Becquart, Phys. Rev. B 65 (2002) 024103.
- [18] M.S. Daw, M.I. Baskes, Phys. Rev. Lett. 50 (1983) 1285.
- [19] M.S. Daw, M. I Baskes, Phys. Rev. B 29 (1984) 6443.
- [20] Documentation du code ASSIMPOT: bases théoriques et utilisation, note interne EDF, HI-23/05/003/A.
- [21] W.H. Press, S.A. Teukolsky, W.T. Vetterling, B.P. Flannery, in: Numerical Recipes, Cambridge University Press, Cambridge, 1992, pp. 418–423.
- [22] O. Talagrand, in: A. Griewank, G. Corliss (Eds.), Automatic Differentiation of Algorithms: Theory, Implementation and Application, SIAM, 1991, pp. 169–180.
- [23] R. Giering, T. Kaminski, ACM Trans. Math. Software 24 (4) (1998) 437.
- [24] G.J. Ackland, M.I. Mendelev, D.J. Srolovitz, S. Han, A.V. Barashev, J. Phys: Condens. Matter 16 (2004) 1.
- [25] G.J. Ackland, D.J. Bacon, A.F. Calder, T. Harry, Philos. Mag. A 75 (1997) 713.
- [26] M.I. Mendelev, S. Han, D.J. Srolovitz, G.J. Ackland, D.Y. Sun, M. Asta, Philos. Mag. 83 (2003) 3977.
- [27] A.D. Le Claire, in: H. Mehrer (Ed.), Numerical Data and Functional Relationships in Science and Technology, Landolt-Börnstein, New Series III, vol. 26, Springer-Verlag, 1990, pp. 480–481.
- [28] S. Takaki, J. Fuss, H. Kugler, U. Dedek, H. Schults, Radiat. Effects 79 (1983) 87.
- [29] J.R. Beeler Jr., in: P.C. Gehlen, J.R. Beeler Jr. (Eds.), Interatomic Potentials and Simulation of Lattice Defects, Plenum Press, New York, 1972.
- [30] R.A. Arndt, A.C. Damask, Acta Metall. 12 (1964) 341.
- [31] M. Wuttig, J.T. Stanley, H. K. Birnbaum, Phys. Status Solidi 27 (1968) 701.
- [32] E.A. Little, D.R. Harries, Metall. Sci. J. 4 (1970) 188.
- [33] A. Vehanen, P. Hautojärvi, J. Johansson, J. Yli-Kauppi, P. Moser, Phys. Rev. B 25 (1982) 762.
- [34] W.K. Choo, R. Kaplow, Acta Metall. 21 (1973) 725.
- [35] R.A. Johnson, A.C. Damask, Acta Metall. 12 (1964) 443.
- [36] D.A. Porter, K.E. Easterling, Phase transformations in Metals and Alloys, Chapman et Hall, 1981, p. 385.
- [37] LAMMPS molecular dynamics software, www.cs.sandia.gov/~sjp-limp/lammps.html.
- [38] L. Cheng, A. Böttgere, Th. H. Keijser, E.J. Mittemeijer, Scripta Metall. Mater. 24 (1990) 509.
- [39] C.A. Wert, Phys. Rev. Lett. 79 (1950) 601.
- [40] M. Weller, J. Phys. (IV) C (8) (1997) 287.
- [41] T. Gladman, The Physical Metallurgy of Microalloyed Steels, Institute of Materials, 1997, p. 206.
- [42] J.L. Snoek, Physica 8 (1941) 711.
- [43] V. Vitek, Cryst. Latt. Def. 5 (1974) 1.
- [44] T. Harry, D.J. Bacon, Acta Mater. 50 (2002) 195.
- [45] C. Domain, G. Monnet, Phys. Rev. Lett. 95 (2005) 215506.
- [46] J.R. Beeler, G.L. Kulcinski, in: P.C. Gehlen, J.R. Beeler, R.I. Jaffee (Eds.), Interatomic Potentials and Simulation of Lattice Defects, Plenum, New York, 1972, p. 735;
- [47] C.H. Bennett, in: A.S. Norwick, J.J. Burton (Eds.), Diffusion in Solids, Recent Developments, Academic, New York, 1975, p. 85.
- [48] K. Kamber, D. Keefer, C. Wert, Acta Metall. 9 (1961) 403.
- [49] A.W. Cochardt, G. Schoek, H. Wiedersich, Acta Metall. 3 (1955) 533.